

Highlights

Physics-Informed Graph Neural Network with Frequency-Aware Learning for Optical Aberration Correction

Yong En Kok, Bowen Deng, Alexander Bentley, Andrew J. Parkes, Michael G. Somekh, Amanda J. Wright, Michael P. Pound

- Physics-informed framework for joint image restoration and aberration prediction.
- Zernike Graph models physical relationships between Zernike modes based on azimuthal degrees.
- Spatial frequency-aware loss enforces consistency in the Fourier domain.
- Outperforms SOTA on CytoImageNet with diverse samples, large-amplitude aberrations.

Physics-Informed Graph Neural Network with Frequency-Aware Learning for Optical Aberration Correction

Yong En Kok^a, Bowen Deng^a, Alexander Bentley^b, Andrew J. Parkes^a, Michael G.
Somekh^{b,c}, Amanda J. Wright^b, Michael P. Pound^{a,*}

^a*School of Computer Science, University of Nottingham, Nottingham, NG8 1BB, Nottinghamshire, United Kingdom*

^b*Optics and Photonics Group, Department of Electrical and Electronic Engineering, University of Nottingham, Nottingham, NG8 1BB, Nottinghamshire, United Kingdom*

^c*Research Center for Humanoid Sensing, Zhejiang Laboratory, Hangzhou, 3111100, Zhejiang, China*

Abstract

Optical aberrations significantly degrade image quality in microscopy, particularly when imaging deeper into samples. These aberrations arise from distortions in the optical wavefront and can be mathematically represented using Zernike polynomials. Existing methods often address only mild aberrations on limited sample types and modalities, typically treating the problem as a black-box mapping without leveraging the underlying optical physics of wavefront distortions. We propose ZRNet, a physics-informed framework that jointly performs Zernike coefficient prediction and optical image Restoration. We contribute a Zernike Graph module that explicitly models physical relationships between Zernike polynomials based on their azimuthal degrees—ensuring that learned corrections align with fundamental optical principles. To further enforce physical consistency between image restoration and Zernike prediction, we introduce a Frequency-Aware Alignment (FAA) loss, which better aligns Zernike coefficient prediction and image features in the Fourier domain. Extensive experiments on CytoImageNet demonstrates that our approach achieves state-of-the-art performance in both image restoration and Zernike coefficient prediction across diverse microscopy modalities and biological samples with complex, large-amplitude aberrations. Code is

*Corresponding author

Email address: michael.pound@nottingham.ac.uk (Michael P. Pound)

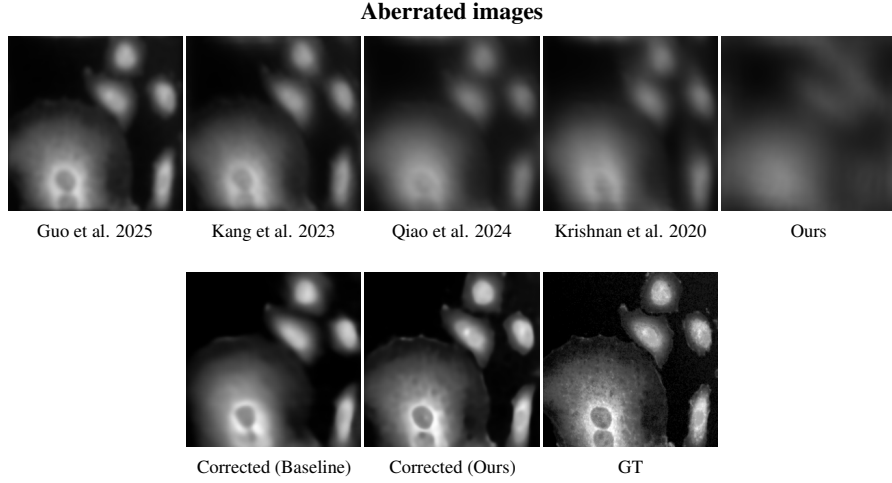


Figure 1: Comparison of aberration severity and correction performance. The top row shows aberrated images: those generated using implementations from previous works and an aberrated image from our approach. Our method applies approximately twice as many Zernike coefficients with larger amplitudes, resulting in a more severely aberrated image. The bottom row displays the corresponding corrected images from the baseline method and our method, respectively, along with the ground truth for reference.

available at <https://github.com/janetkok/ZRNet>.

Keywords: , Adaptive Optics, Aberration Correction, Deep Learning

1. Introduction

High-resolution optical imaging is essential across a variety of fields, particularly medical, astronomical and microscopic imaging [1]. However, optical imaging quality is often degraded by system and sample-induced wavefront aberrations. System-induced aberrations arise from manufacturing or assembly imperfections, whereas sample-induced aberrations stem from variations in refractive index of the specimen [2]. To improve optical imaging quality, Adaptive Optics (AO) has emerged as a powerful technique to correct these aberrations, in which the aberration is first quantified before a corrective phase pattern is applied to the wavefront. Aberrations are typically represented as a weighted linear combination of Zernike polynomials, and the challenge of accurately determining which Zernikes are present when imaging deep into a sample has existed

for decades. While traditional AO approaches using a wavefront sensor [3, 4] offer high-speed aberration measurement, they typically require a known reference point in the sample, complicating preparation and limiting applicability to complex specimens where introducing exogenous references is impractical [5]. Sensorless AO has emerged as a cost-effective alternative, advancing from classical iterative optimisation methods [6, 7, 8, 9, 10] to more recent deep learning approaches.

Deep learning methods have shown promise in directly reconstructing aberration phases [11, 12, 13] and recovering the Zernike coefficients [14, 15, 16, 17, 18] from input aberrated intensity images. However, these methods still require an additional step of applying corrective aberrations to the optical system or post-processing through deconvolution algorithms [19, 20], which can introduce artifacts due to inaccurate Point Spread Function (PSF) [21] estimation. While parallel work in direct image restoration [22] offers instant visualisation, it risks generating hallucinations in heterogeneous specimens. Thus, researchers have begun to shift toward hybrid approaches that combine deep learning with physical priors that enhance correction reliability [23, 24, 25].

The challenge increases substantially when imaging deeper into samples, where aberrations become more complex and severe. Deeper tissue imaging introduces compound aberrations where different Zernike modes become strongly coupled, necessitating both a larger number of modes for correction and greater amplitude compensation [26, 27]. Critically, most existing deep learning methods in this field [23, 24, 25] are limited to addressing low-order Zernike modes at relatively small amplitudes. While a useful proof of concept, this underestimates the size of aberrations in tissue samples [28]. Imaging deep remains a challenge in optical microscopy, with many instruments struggling to image beyond a few hundred micrometers deep and overcoming this problem would transform the field. In contrast, our work tackles substantially more complex cases by handling roughly double the number of Zernike modes at approximately twice the amplitude of previous approaches (see Fig. 1 for an illustration of the amount of aberration applied in each work). Furthermore, most existing approaches typically focus on single imaging modalities and specific cell types, leaving their generalisability to different microscopy techniques, multiple objects in the field of view, and diverse biological samples uncertain. We instead evaluate our work on CytoImageNet dataset [29], a

large-scale compilation of 40 publicly available microscopy datasets spanning multiple imaging modalities and varied biological classes (e.g., nuclei, mitochondria, etc.).

In natural images, state-of-the-art (SOTA) architectures have excelled in tasks such as denoising [30, 31, 32], deblurring [33, 34, 35], and super-resolution [36]. These methods have proven effective, but typically tackle simpler, more uniform distortions (e.g., motion or defocus blur) and seldom account for the complex interactions of optical distortions across the image field.

In this work, we propose a physics-informed framework that jointly solves the problem of Zernike coefficient prediction and optical image restoration. A key innovation is the integration of a novel Zernike Graph Neural Network (GNN) that explicitly models the physical relationship between groups of Zernike coefficients, enabling the model to learn an appropriate correction. By jointly optimising the image restoration network and Zernike graph module for accurate Zernike prediction, we impose physics-based constraints that guide the network to couple denoising with aberration correction, leveraging the underlying physics that governs how different Zernike modes interact and influence image quality.

To enforce physical consistency between image restoration and Zernike prediction, we introduce the Frequency-aware Alignment (FAA) loss. Operating in the spatial Fourier domain where optical aberrations distinctly manifest and high spatial frequencies correspond to fine image detail. This loss function ensures that the predicted Zernike coefficients correspond to actual restorative transformations rather than dataset-specific artifacts. Our approach bridges the gap between image restoration and aberration prediction while promoting more reliable and generalisable solutions.

We demonstrate SOTA performance on a diverse range of microscopy images against both leading image restoration models, and leading aberration correction models. Our primary contributions are:

- We propose Zernike coefficient prediction and optical image Restoration Network (ZRNet), a physics-informed framework that unifies image restoration and aberration estimation. We introduce a novel Zernike Graph Neural Network that explicitly encodes the non-linear coupling between Zernike modes based on their

azimuthal degrees, ensuring the learned latent representations adhere to physical optical principles.

- We formulate a FAA loss function to enforce consistency between the restoration and prediction branches. By operating in the Fourier domain, this mechanism penalises phase and amplitude distortions, effectively bridging the domain gap between pixel-wise restoration and Zernike coefficient regression.
- We demonstrate that our joint optimisation strategy significantly improves generalisation across varied biological samples and microscopy modalities. Extensive evaluations on CytoImageNet show that ZRNet achieves SOTA performance, specifically in correcting high-order, large-amplitude aberrations where previous methods typically fail.

2. Related Work

2.1. Image Restoration Networks.

Image restoration aims to recover high-quality images from degraded inputs. Deep learning approaches have revolutionised this field with advances in deblurring [33, 34], denoising [30, 31, 32], dehazing [37, 38, 39], and super-resolution [40, 41, 42] tasks, enabling reliable recovery of image features across diverse degradation conditions. For a comprehensive survey of deep learning-based image restoration methods, we refer readers to [43]. Modern image restoration approaches predominantly employ encoder-decoder architectures [32, 35], which learn compressed representations while preserving fine detail through skip connections [44]. To further enhance restoration quality, various architectural innovations have been proposed, including channel attention [45, 46], spatial attention [47, 48], kernel-based attention [49], non-local operations [50], multi-scale processing [51], and multi-stage refinement [33].

More recently, generative networks such as Generative Adversarial Network (GAN)s [34, 41] and diffusion models [35] have been developed to more effectively handle complex degradations. These frameworks learn the underlying image distribution to enable higher quality restorations through either adversarial training or iterative

denoising respectively. Despite producing visually appealing results, GANs are prone to mode collapse and training instability, while diffusion models face challenges with computational overhead and error accumulation during iterative sampling steps [52, 53]. Other approaches have applied transformer-based architectures to good effect [32, 31], leveraging their ability to model long-range dependencies and global context through self-attention.

While these architectural innovations effectively handle common image degradations such as defocus blur, motion blur, and Gaussian noise — these distortions tend to be more uniform and predictable. In contrast, optical aberrations pose unique challenges through intricate, depth-dependent, and spatially varying wavefront distortions that interact in complex ways across the image field. Robust aberration correction demands simultaneous understanding of wavefront behaviour and advanced restoration techniques, motivating the integration of sophisticated deep learning techniques with physics-informed frameworks for aberration correction.

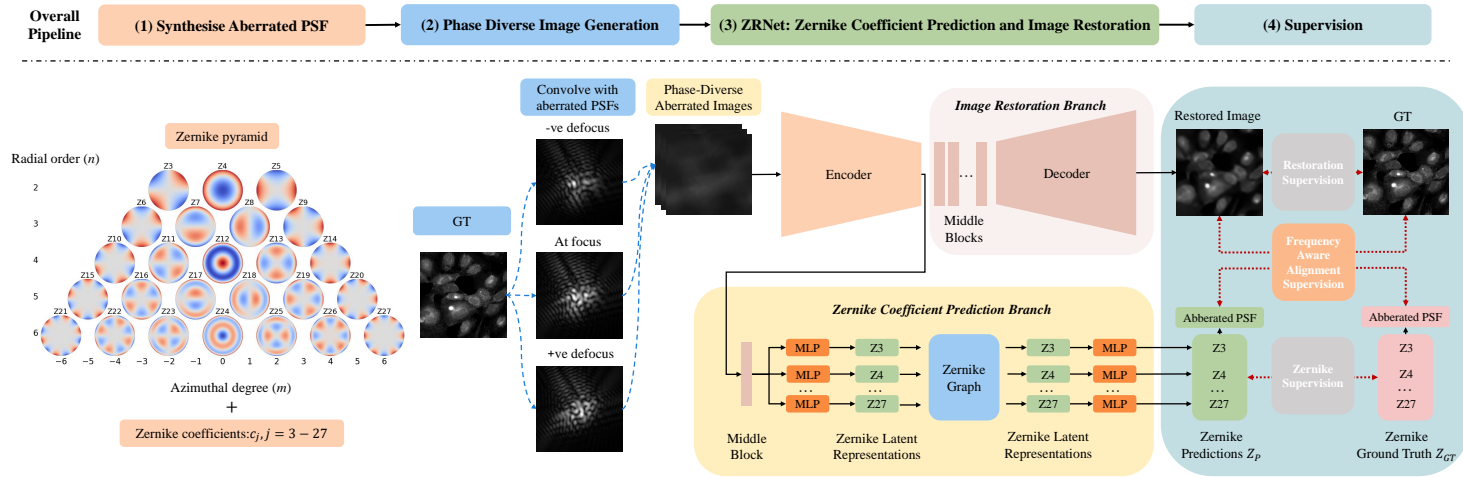


Figure 2: Overall pipeline: (1) synthesis of aberrated PSFs using Zernike polynomials, (2) generation of phase-diverse images by convolving ground truth samples with aberrated PSFs across multiple focal planes, (3) ZRNet that simultaneously restores images and predicts Zernike coefficients in a single forward pass, (4) with supervision across three domains: image space, frequency space, and Zernike coefficients.

2.2. *Direct Optical Aberration Correction using Deep Learning.*

Research on direct optical aberration correction using deep learning is less established. While approaches such as Guo et al. [22] demonstrate the effectiveness of solely using deep learning architectures for direct mapping between degraded and high-quality optical images, their method showed negligible improvement beyond 4th order Zernikes and risked hallucinations with heterogeneous specimens. This has prompted researchers to shift toward hybrid approaches that combine deep learning with physical priors to enhance correction reliability through consistency loss mechanisms. For instance, Krishnan et al. [23] implemented a dual-network architecture that simultaneously optimises image restoration and Zernike coefficient estimation, but struggled with higher-order aberrations and showed no clear benefits from joint training and the consistency loss. Similar consistency mechanisms have been adopted by Kang et al. [24], who developed a self-supervised algorithm using coordinate-based neural representations to jointly estimate Zernike coefficients and recover 3-dimensional structure in widefield microscopy images, but this work only addressed 1-3 Zernike coefficients. Qiao et al. [25] proposed a two-stage architecture where a dual-branch network, consisting of spatial and Fourier domain feature extraction paths, first estimates optical aberrations, with this aberration estimation then serving as input to guide a separate aberration-aware super-resolution network for image restoration. The authors observed that incorporating higher-order aberrations significantly degraded performance, even at the aberration estimation stage, which could potentially misdirect the subsequent image restoration process.

While progress has been made, image restoration of large amplitude aberration, common in tissue samples at increasing depth, has yet to be solved. Our work addresses this challenge, with higher-order aberrations (up to 6th order, 25 Zernike coefficients) at larger amplitudes. Moreover, we uniquely incorporate explicit modelling of the physical relationships between aberration modes, providing valuable constraints for more accurate estimation and correction. This broader scope and deeper physical integration represents a significant departure from previous approaches, tackling more challenging optical aberration scenarios.

3. Aberration Dataset

3.1. Aberrated Point Spread Function (PSF).

Optical aberrations in an imaging system, such as a microscope, can be modeled using its point spread function (PSF). The PSF describes how the imaging system responds to a single point source of light and represents the system's spatial resolution. In an ideal system, the PSF is a diffraction-limited single point of finite size and shape, while aberrations in real systems further distort it [54], degrading image quality. The PSF is calculated by taking the Fourier transform of the complex pupil function, which defines how light is transmitted through an optical system:

$$PSF(x, y) = \left| \mathcal{F}\{A(x, y) \exp(i\phi(x, y))\} \right|^2 \quad (1)$$

where, $A(x, y)$ is a circular aperture mask (1 inside, 0 outside), ϕ is the wavefront phase and \mathcal{F} is the Fourier transform.

To model the wavefront phase ϕ , we use Zernike polynomials, which provide a complete mathematical basis for describing wavefront aberrations. These polynomials can be defined as either odd or even functions:

$$Z_n^m(\rho, \phi) = R_n^m(\rho) \cos(m\phi) \quad (2)$$

and odd polynomials given by:

$$Z_n^{-m}(\rho, \phi) = R_n^m(\rho) \sin(m\phi) \quad (3)$$

where R_n^m is a radial polynomial dependent on m , n and the radial distance ρ and ϕ is the azimuthal angle. Zernike polynomials are particularly useful because they are orthogonal over a unit circle [55] and can be grouped by radial order (n), azimuthal degree (m), or aberration type to collectively model different types of optical distortions (see Zernike pyramid in Fig. 2).

In this work, the wavefront phase ϕ is defined through the linear combination of weighted Zernike polynomials 3-27 (ANSI indices), Z_j in Eqn. 4, excluding Z_0 (piston), Z_1 (tip), and Z_2 (tilt) modes as they can be corrected using standard centroiding or registration methods.

$$\phi(x, y) = \sum_{j=3}^{27} c_j Z_j(x, y) \quad (4)$$

where c_j are coefficients randomly sampled from a uniform distribution within $[-1, 1]$ rad.

3.2. Phase-Diverse Image Generation.

Following previous work [23, 56, 57], we use phase-diverse images captured at multiple focal planes as input. The use of phase-diversity has been known to enhance models employing Zernikes by resolving the inherent ambiguity present in certain Zernike polynomials when looking at an image taken at a single focal plane. To generate our phase-diverse dataset, each sample image is convolved with an aberrated PSF at three defocus levels: negative defocus (-1 rad), at-focus (0), and positive defocus ($+1$ rad), as illustrated in Fig. 2.

4. Methodology

In this section, we first delineate the overall architecture of ZRNet. Then we describe the proposed Zernike graph module and the Frequency-Aware Alignment (FAA) loss.

4.1. Overall Pipeline

As illustrated in Fig. 2, the proposed ZRNet processes phase-diverse aberrated images through two parallel branches: (1) An encoder-decoder architecture that employs KBNets₅ [49] as its backbone for image restoration, and (2) a Zernike coefficient prediction branch featuring our Zernike Graph that enforces physical constraints by learning the established interactions between Zernike modes to decipher the nature of the aberration. The two branches mutually reinforce each other, compelling the image restoration to adhere to underlying optical properties while the restoration objective regularises Zernike coefficient estimation.

4.2. Zernike Graph

While Zernike polynomials are mathematically orthogonal when describing the optical field, the microscope is sensitive to intensity (the square of the field), which effectively breaks down this orthogonality. We thus hypothesise that explicitly exploiting correlations among Zernike modes will improve aberration correction performance.

Standard deep learning approaches typically employ a fully connected layer to directly map the latent features extracted by the image encoder to the Zernike coefficients. This formulation effectively linearises the Zernike space into a flat, unstructured Euclidean vector, implicitly assuming that the modes are independent regression targets. Consequently, these models lack the structural capacity to explicitly model the conditional dependencies between coefficients, forcing the network to learn complex physical couplings entirely from data without architectural guidance.

In contrast, we argue that the non-linear coupling between Zernike modes is best modelled as a graph structure, where edges explicitly encode physical interactions based on Zernike mode groupings. To harness this topology, we leverage GNNs, specifically Graph Attention (GAT) [58], which excel at modelling inter-relationships through message passing between connected nodes. Inspired by QAGNet [59], we propose a grouped GNN approach that moves beyond simple independent regression to reason about the aberration composition. Our approach achieves this by harnessing the dependencies both within natural Zernike groups and the global interactions between these groups. We consider two primary grouping strategies, and a baseline in which no grouping is applied:

Azimuthal Degree Grouping. Zernike modes sharing the same azimuthal degree (m) have identical angular periodicity and symmetry. For example, vertical trefoil (Z6, $m=-3$) and vertical secondary trefoil (Z16, $m=-3$) collectively define a triple-angle sine variation, making them naturally suited for joint processing.

Aberration Grouping. Organises Zernike polynomials based on the physical aberrations they represent in optical design. By grouping aberrations this way, Zernikes with the same radial order (n) and same absolute azimuthal degree (m) are assigned to the same class where their corresponding polynomials are identical with a $\pi/2$ phase shift. For instance, Z11 ($n = 4, m=-2$) and Z13 ($n=4, m=2$) together contribute to secondary astigmatism, creating a physically meaningful category for targeted aberration correction.

Our ablation studies indicate that organising Zernike polynomials by azimuthal degree yields superior results; hence, we focus on this strategy in our primary experiments. Further details regarding the aberration grouping and baseline are provided in

the appendix.

As illustrated in Fig. 3, the Zernike graph module operates in a hierarchical four stages process designed to model the physical relationships of aberrations:

(1) Node Initialisation and Intra-Group Interaction. First, the latent features extracted by the image encoder are projected into mode-specific representations via separate Multi-Layer Perceptron (MLP). Let $\mathcal{H} = \{h_3, \dots, h_{27}\}$ denote this set of latent feature vectors, which serve as the initialisation for the corresponding Zernike graph nodes. To capture local symmetry constraints, Zernike nodes are first partitioned into subsets S_m based on their azimuthal degree $m \in M = \{-6, \dots, 6\}$. For each subset, let \mathbf{H}_{S_m} denote the feature matrix constructed by stacking the latent vectors $\{h_i \mid i \in S_m\}$. Within each group, a single GAT layer updates the features by modelling the intra-group dynamics. This deliberate choice of a single layer maintains a lean architecture that models the physical relationships of Zernike polynomials while achieving diffraction-limited performance:

$$\hat{\mathbf{H}}_{S_m} = \text{GAT}(\mathbf{H}_{S_m}, A_{intra}) \quad (5)$$

where $\hat{\mathbf{H}}$ denotes the updated feature matrix and A_{intra} represents the fully connected adjacency matrix within the group.

(2) Group Aggregation via Proxy Nodes. To capture the collective behaviour of each distinct angular variation, we aggregate the information within each subset S_m into a unified proxy node p_m . This process consists of two steps. First, the proxy node is initialised as p_m^0 by averaging the original latent features \mathbf{H}_{S_m} :

$$p_m^0 = \text{Mean}(\mathbf{H}_{S_m}) \quad (6)$$

Next, to refine this representation, we employ a directed message passing step where information flows from the updated constituent Zernike nodes ($\hat{\mathbf{H}}_{S_m}$) to the proxy:

$$p_m = \text{GAT}(p_m^0, \hat{\mathbf{H}}_{S_m} \mid A_{agg}) \quad (7)$$

where A_{agg} defines directed edges from the Zernike nodes to their respective proxy node. For singleton groups (e.g., Z15 for vertical pentafoil, $m = -5$), the node feature is directly assigned as the proxy.

(3) Global Inter-Group Exchange. To model the complex interaction between different angular symmetry patterns and how they influence each other within the optical system, the proxy nodes form a fully-connected graph. Let \mathbf{P} denote the feature matrix constructed by stacking the proxy nodes $\{p_m \mid m \in M\}$. A GAT layer then facilitates the inter-group exchange:

$$\hat{\mathbf{P}} = \text{GAT}(\mathbf{P}, A_{\text{global}}) \quad (8)$$

where A_{global} represents the fully connected adjacency matrix.

(4) Hierarchical Feedback and Prediction. The processed group-level information is fed back to individual Zernike nodes to generate refined latent representations. To obtain the final coefficients, these refined features are passed through separate MLPs to predict the final Zernike coefficients. This hierarchical approach ensures the framework respects both local relationships within azimuthal degree groups and global interactions between different angular symmetry variations, leading to more accurate and physically consistent predictions.

4.3. Loss Function

Traditional image restoration networks typically optimise an L_1 loss between the restored and ground truth images. Our framework extends this by introducing a parallel objective that minimises the Mean Squared Error (MSE) between predicted and ground truth Zernike coefficients - fundamental optical descriptors that characterise wavefront aberrations. While this additional term helps guide the restoration process by leveraging aberration information encoded in the Zernike polynomials, optimising these losses independently can lead to physically inconsistent solutions. The network may learn shortcuts that, while effective on the training set, fail to capture the underlying optical physics and thus generalise poorly.

To address this limitation, we introduce the FAA loss to enforce consistency between image restoration and Zernike prediction through a three-way interconnected supervision system. By computing the loss in the Fourier domain, the network directly penalises errors in the spatial frequency components most affected by aberrations and increases sensitivity to both phase and amplitude distortions. The loss ensures the network learns physically meaningful image restorative transformations, while simultaneously

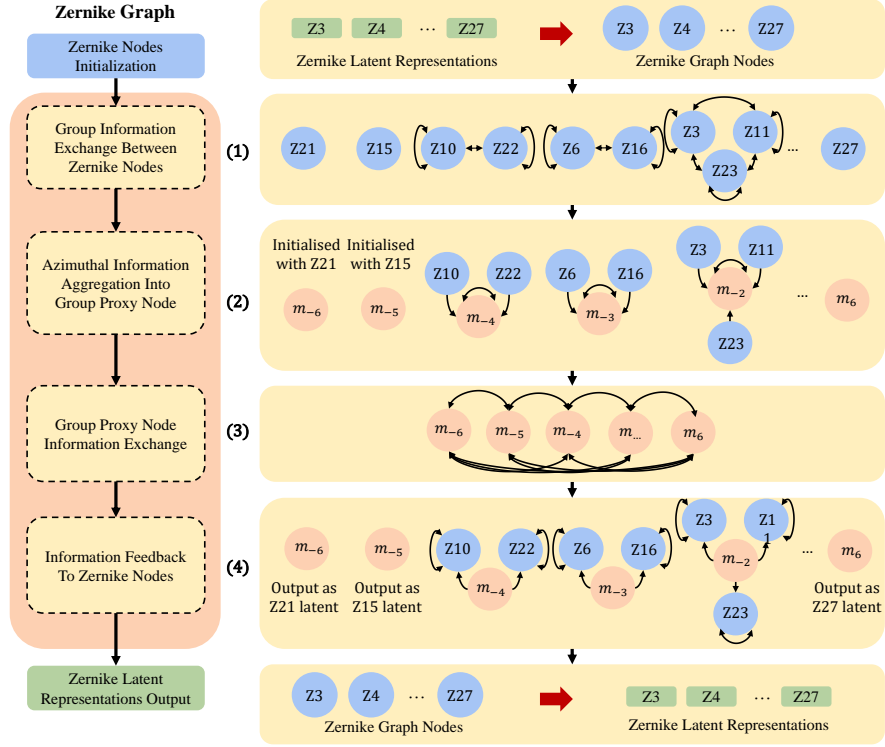


Figure 3: Our Zernike graph architecture for processing Zernike modes based on their azimuthal degrees. The framework processes information in four stages: (1) Node initialisation and intra-group exchange between Zernike nodes sharing the same azimuthal degree, (2) Information aggregation within each azimuthal degree group, (3) Inter-group information exchange via a fully-connected graph between different azimuthal degree groups, and (4) Information feedback to individual Zernike nodes to generate final latent representations.

predicting Zernike coefficients that correspond to the actual restoration process, leading to improved generalisation and more reliable aberration correction. The FAA loss is formulated as:

$$L_{\text{FAA}} = L_R + L_C + L_Z \quad (9)$$

where the three complementary terms in the equations enforce consistency in the frequency domain. Let $\mathcal{F}(x)$ denote the Fourier transform of x , $A(Z)$ represents the aberrated PSF generated from Zernike coefficients Z , I_R and I_{GT} be the restored and

ground truth images respectively, and Z_P and Z_{GT} denote the predicted and ground truth Zernike coefficients. The operator \circledast represents the convolution of the aberrated PSF with an image.

Each loss term computes the L_1 norm of both real (Re) and imaginary (Im) components separately in Fourier space, providing a numerically stable and computationally efficient way to capture frequency domain differences.

1. **Restoration Loss (L_R):** The restoration loss ensures that the restored image, when re-aberrated with ground truth Zernikes, matches the original aberrated image in frequency space.

$$L_R = \sum_{p \in \{Re, Im\}} |p(\mathcal{F}(I_R \circledast A(Z_{GT})) - \mathcal{F}(I_{GT} \circledast A(Z_{GT})))| \quad (10)$$

2. **Cross-verification Loss (L_C):** Cross-verification loss bridges image restoration and Zernike prediction tasks by comparing the effects of ground truth Zernikes applied to the restored image against predicted Zernikes applied to the ground truth image, enforcing mutual consistency between the two tasks.

$$L_C = \sum_{p \in \{Re, Im\}} |p(\mathcal{F}(I_R \circledast A(Z_{GT})) - \mathcal{F}(I_{GT} \circledast A(Z_P)))| \quad (11)$$

3. **Zernike Loss (L_Z):** This loss assesses the accuracy of predicted Zernikes by comparing their effects with those of ground truth Zernikes when applied to the ground truth image.

$$L_Z = \sum_{p \in \{Re, Im\}} |p(\mathcal{F}(I_{GT} \circledast A(Z_{GT})) - \mathcal{F}(I_{GT} \circledast A(Z_P)))| \quad (12)$$

The final total loss is defined as:

$$L_{\text{total}} = L_1(I_{GT}, I_R) + \lambda_1 MSE(Z_{GT}, Z_P) + \lambda_2 L_{\text{FAA}}(I_{GT}, I_R, Z_{GT}, Z_P) \quad (13)$$

where $\lambda_1 = 0.5$ and $\lambda_2 = 0.01$ are weighting factors determined through grid search to balance the contributions of the loss terms.

5. Experiments

5.1. Experimental Setup

5.1.1. Dataset

To demonstrate our model generalisation across diverse biological samples and microscopy modalities, we utilised CytoImageNet [29], a large-scale dataset designed for bioimage transfer learning, compiled from 40 openly available datasets within: Recursion, Image Data Resource (IDR) [60], Broad Bioimage Benchmark Collection (BBBC) [61], Kaggle, and Cell Image Library (CIL). The dataset comprises approximately 890k grayscale microscopy images across 894 classes, spanning fluorescence, confocal, brightfield, light, and darkfield modalities.

We train on the CytoImageNet training set of approximately 801k images. For efficient evaluation, we randomly select 20k images from the large validation set for our validation and another 20k images for testing. All sample images were resized to 256×256 pixels before convolution with aberrated PSFs to generate our phase-diverse dataset.

5.1.2. Evaluation Metrics

For image restoration, we report standard image metrics PSNR [62], SSIM [63] and LPIPS [64] between the restored image and ground-truth images, and use calflops [65] to calculate the floating-point operations (FLOPs) for each model. To assess the accuracy of the Zernike predictions, we follow established methods [15, 17] in adaptive optics to use Root Mean Square Wavefront Error (RMS_{WFE}) to quantify the residual wavefront error that would remain after correction by subtracting the predicted Zernike modes, Z_P from the ground truth Zernike modes, Z_{GT} :

$$RMS_{WFE} = \sqrt{\sum_{j=1}^M \frac{1}{N} \sum_{i=1}^N (Z_{P_{ij}} - Z_{GT_{ij}})^2} \quad (14)$$

where N is the number of samples and M is the number of Zernike modes. A $RMS_{WFE} < 0.45$ rad is generally considered indicative of diffraction-limited imaging performance [66].

5.1.3. Implementation Details

We implement and train our models on phase-diverse aberrated images using a single NVIDIA RTX A6000 GPU with batch size 8. During each training iteration, Zernike coefficients are randomly sampled to generate aberrated PSF kernels, which are then convolved with optical images from the training dataset. Following KBNet_s [49] configuration, we train the model using fixed 256×256 images and the AdamW optimizer. We employ a cosine annealing scheduler with warm restarts. The learning rate is fixed at 3e-4 for the first 300k iterations, after which the scheduler begins warm restarts every 208k iterations with the learning rate decaying to a minimum of 2.5e-5.

Our training strategy consists of two phases: (1) We first pretrain the autoencoder and the initial MLPs for 250k iterations, which excludes the Zernike graph and the final MLP components. During this phase, the network learns direct Zernike coefficient prediction through the MLPs rather than generating latent representations for graph processing. This pretraining strategy is helpful as it allows the encoder-decoder backbone and coefficient prediction branches to establish robust feature representations prior to the introduction of more complex graph-structured learning. In contrast, training the full model from scratch without these prelearned features leads to unstable optimisation, where we observed loss divergence after approximately 60k iterations. During the pretraining stage, we exclude the FAA loss as initial Zernike predictions can be noisy and inconsistent, making any consistency constraints through the FAA loss counter-productive for training stability. (2) We then fine-tune the complete ZRNet framework for 1350k iterations, including the Zernike graph component, using identical training parameters and the complete loss function defined in Eq. 13.

5.2. Comparison with the State-Of-The-Art

We compare the proposed ZRNet with several SOTA image restoration and aberration correction networks: DeblurGANv2 [34], DeAbe (RCAN) [22, 45], SFT-DFCAN [25], MPRNet [67], Restormer [32], CascadedGaze [68], DiffIR [35], and KBNet (both large KBNet_L and small KBNet_s variants) [49].

For Zernike coefficient prediction, we established a baseline using a variant of ZRNet without the image restoration component (ZRNet w/o image restoration). We

also compared our framework against Swin Transformer [69].

To ensure fair comparison, we trained and evaluated all competing methods on the same dataset following their original configurations with minimal task-specific adaptations, and trained for identical durations as our approach. For each method, we selected the best-performing model based on validation set performance and report results from evaluating these models on our held-out test set. Detailed implementation specifications are provided in the appendix.

5.2.1. Quantitative Comparison

We present quantitative comparisons of image restoration in Tab. 1. Our method achieves the highest scores across all metrics, outperforming existing image restoration networks. Benefiting from physics-guided aberration modelling, our approach demonstrates superior pixel-wise accuracy (PSNR) and perceptual quality (SSIM, LPIPS), surpassing the second-best method KBN_{Net_L} by 7.62%, 6.27%, and 9.94% respectively, while requiring 34.6% fewer FLOPs due to our use of a smaller backbone.

For Zernike coefficient prediction (Table 2), ZRNet reduces the initial aberration from an average RMS_{WFE} of 2.8867 rad to 0.4374 rad, achieving diffraction-limited performance and outperforming other baselines. The joint training with image restoration substantially improves aberration characterisation, reducing the error by 18% compared to the ablated variant (ZRNet w/o image restoration), highlighting the critical contribution of the image restoration branch for precise Zernike coefficient predictions. Even without image restoration, ZRNet outperforms Swin transformer, demonstrating the effectiveness of our GNN architecture.

5.2.2. Qualitative Comparison

Figure 4 demonstrates qualitative comparisons with SOTA methods on diverse cellular samples. Under severe optical aberrations, our method shows great improvement in restoration quality, preserving fine cellular details while other methods introduce artifacts or retain residual blur. Our restorations more closely match the ground truth, particularly in preserving cell morphology and intensity distributions. Corresponding Zernike coefficient predictions are presented in Fig. 5. In all cases, ZRNet accurately

Method	PSNR	SSIM	LPIPS	FLOPs (G)
<i>General image restoration networks</i>				
DeblurGANv2	22.28	0.5659	0.5187	51.06
MPRNet	23.47	0.6528	0.5088	1536.08
Restormer	23.62	0.6545	0.5027	282.01
CascadedGaze	24.59	0.6701	0.4953	123.73
DiffIR	25.42	0.7039	0.4610	225.41
KBNet _S	26.22	0.7221	0.4512	137.62
KBNet _L	26.76	0.7380	0.4316	215.72
<i>Aberration correction networks</i>				
DeAbe (RCAN)	21.30	0.5951	0.5599	513.35
SFT-DFCAN	22.07	0.6113	0.5454	316.07
ZRNet (Ours)	28.80	0.7843	0.3887	141.07

Table 1: Quantitative results of image restoration on CytoImageNet [29]. The images were convolved with optical aberrations with average RMS_{WFE} of 2.8867 rad. Best results are highlighted in bold.

compactness

Method	Zernike RMS_{WFE} (rad)	FLOPs (G)
Swin-B	1.8846	39.58
Swin-L	1.7576	88.97
ZRNet (w/o image restoration)	0.5373	66.22
ZRNet	0.4374	141.07

Table 2: Quantitative results of Zernike coefficient prediction on CytoImageNet [29]. The images were convolved with optical aberrations with average RMS_{WFE} of 2.8867 rad. Best results are highlighted in bold.

predicts both low and high-order Zernike modes, resulting in effective wavefront error reduction and consistent near diffraction-limited correction across diverse aberration patterns.

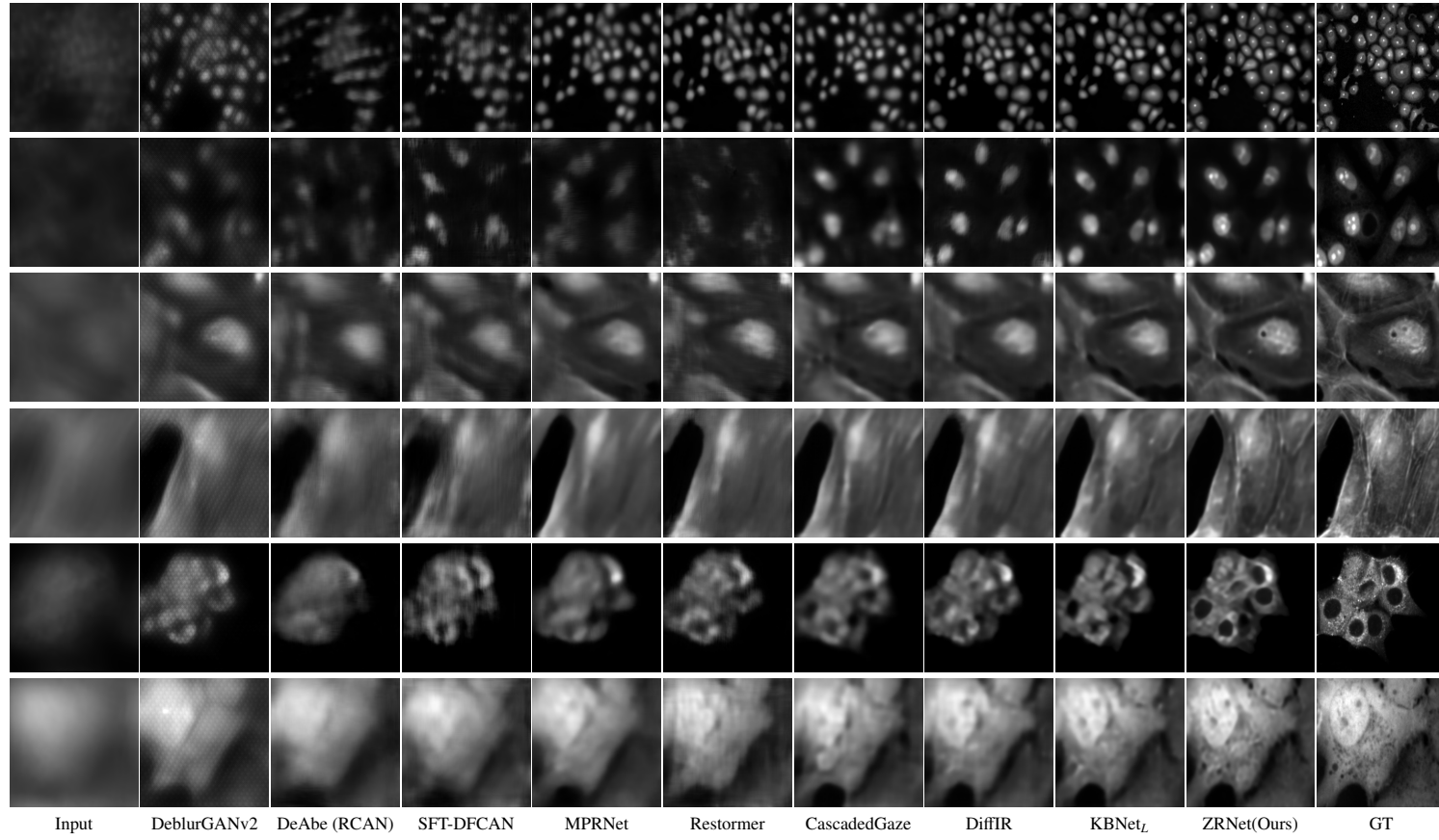


Figure 4: Qualitative comparison of SOTA image restoration networks on CytoImageNet [29] with optical aberration applied. ZRNet exhibits a higher level of fine detail after reconstruction, closer to the ground truth images.

Set	Image restoration branch	FAA loss	Zernike coefficient prediction				PSNR	SSIM	LPIPS	Zernike RMS _{WFE} (rad)
			MLP only	Zernike graph						
				No grouping	Aberration group	Azimuthal degree				
I					✓	NA	NA	NA	0.5373	
II	✓					26.22	0.7221	0.4512	NA	
III	✓		✓			27.70	0.7591	0.4159	1.6109	
IV	✓	✓	✓			27.34	0.7500	0.4226	2.6799	
V	✓				✓	28.48	0.7774	0.3962	0.4471	
VI	✓	✓		✓		28.36	0.7744	0.3991	0.4652	
VII	✓	✓			✓	28.60	0.7796	0.3939	0.4624	
VIII	✓	✓			✓	28.80	0.7843	0.3887	0.4374	

Table 3: Ablation analysis of different modules in ZRNet.

5.3. Ablation Studies

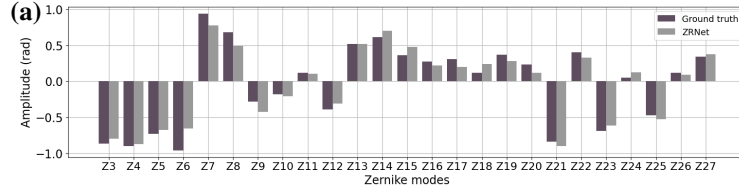
Table 3 presents our ablation analysis of the proposed designs.

5.3.1. Joint Training Benefit

Removing the image restoration branch (Set I) hinders the network from learning how aberrations affect image quality, resulting in worse performance compared to Set V, thus confirming that image restoration provides essential supervision for accurate Zernike prediction through its physical constraints. Even with a suboptimal MLP only Zernike predictor (Set III and IV), joint training yields higher image quality metrics than restoration-only (Set II). This indicates that even imperfect Zernike coefficient predictions provide valuable guidance. Upgrading to our Zernike graph architecture (Sets V-VIII) further enhances restoration performance, demonstrating the mutual benefits between aberration estimation and image restoration.

5.3.2. Effectiveness of FAA Loss

Applying the FAA loss to the MLP-only model (Set III vs IV) is counterproductive, as imposing a strict, physics-driven consistency constraint on the relatively noisy and naive MLP predictions creates a conflicting optimisation problem. In contrast, the full potential of FAA loss is realised when combined with Zernike graph (Set V vs VIII),

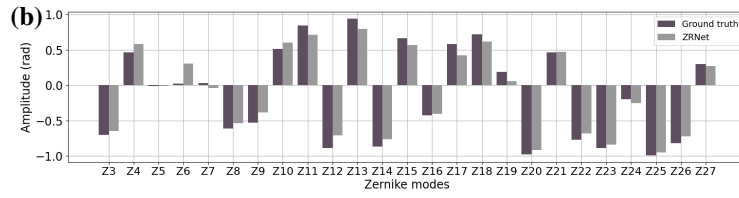


Pre-correction RMS_{WFE} :

2.7361 rad

After correction RMS_{WFE}

ZRNet: 0.5411 rad

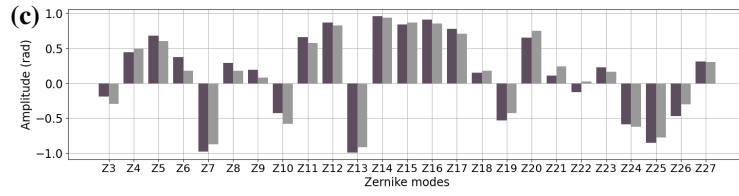


Pre-correction RMS_{WFE} :

3.2570 rad

After correction RMS_{WFE}

ZRNet: 0.5576 rad

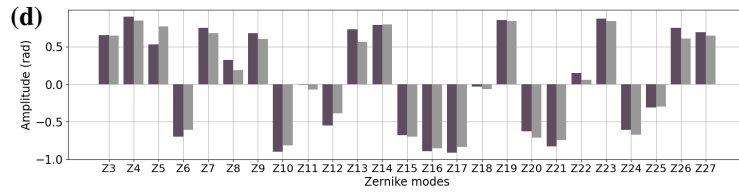


Pre-correction RMS_{WFE} :

3.0865 rad

After correction RMS_{WFE}

ZRNet: 0.4901 rad

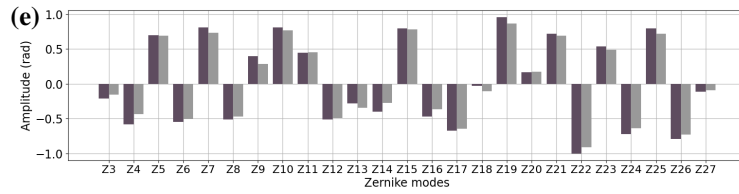


Pre-correction RMS_{WFE} :

3.4027 rad

After correction RMS_{WFE}

ZRNet: 0.4698 rad

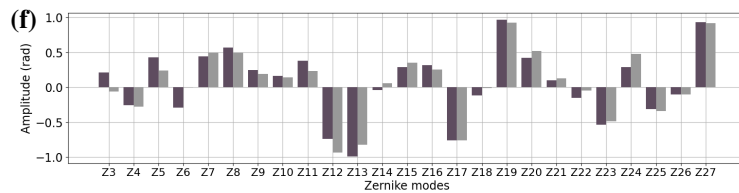


Pre-correction RMS_{WFE} :

3.0777 rad

After correction RMS_{WFE}

ZRNet: 0.3511 rad



Pre-correction RMS_{WFE} :

2.4364 rad

After correction RMS_{WFE}

ZRNet: 0.6199 rad

Figure 5: Zernike coefficients prediction comparing ground truth to ZRNet predictions.

which is explicitly designed to model relationships among Zernike modes and produce more coherent predictions, allowing FAA loss to function synergistically. Ablation studies for each of the FAA loss components, validating our three-way design, are provided in the appendix.

5.3.3. Importance of Zernike Graph

The addition of the Zernike graph in Set VIII leads to substantial improvements across all metrics, most notably in Zernike coefficient prediction when compared to Set IV. Crucially, this performance boost incurs negligible computational overhead, adding only 3.45 GFLOPs to the $KBNet_S$ backbone. This confirms that the structured Zernike graph better captures the relationship than the simple MLP with minimal additional complexity.

5.3.4. Effect of Zernike Polynomial Groupings in Zernike Graph

In Sets VI to VIII, we include the FAA loss and analyse the different Zernike polynomial groupings in the Zernike graph. The results show that both physics-inspired grouping approaches (Sets VII and VIII) perform more effectively than no grouping (Set VI) across all image evaluation metrics, suggesting that structured Zernike relationships enhances restoration quality. Overall, grouping by azimuthal degree (Set VIII) achieves the best performance, indicating this approach better captures the optical principles governing wavefront behaviour and validating our hypothesis that modelling Zernike mode correlations is an effective strategy for aberration correction.

6. Conclusion

In this work, we proposed ZRNet, a physics-informed framework that enables reliable optical image restoration with simultaneous Zernike coefficient prediction. We introduced a GNN-based Zernike graph architecture to model physical relationships between Zernike modes based on their azimuthal degrees, along with the FAA loss to enforce consistency between image reconstruction and aberration prediction in the frequency domain. Extensive experiments demonstrate that our approach effectively models the complex relationship between the Zernike polynomials and achieves SOTA

performance across diverse microscopy modalities and biological samples in CytoImageNet. We believe this work establishes a new direction for integrating physical principles with deep learning for optical imaging applications.

CRedit authorship contribution statement

Yong En Kok: Conceptualization, Data curation, Formal analysis, Investigation, Methodology, Project administration, Software, Validation, Visualization, Writing – original draft, Writing – review and editing. **Bowen Deng:** Formal analysis, Investigation, Methodology, Visualization, Writing – review and editing. **Alexander Bentley:** Formal analysis, Investigation, Writing – review and editing. **Andrew J. Parkes:** Formal analysis, Supervision, Writing – review and editing. **Michael G. Somekh:** Formal analysis, Supervision, Software, Writing – review and editing. **Amanda J. Wright:** Formal analysis, Supervision, Writing – review and editing. **Michael P. Pound:** Conceptualization, Formal analysis, Project administration, Supervision, Writing – review and editing.

7. Funding

This work was supported by the Engineering and Physical Sciences Research Council (EP/T020997/1) and University of Nottingham PhD studentship.

Declaration of competing interest

The authors declare that they have no known competing financial interests or personal relationships that could have appeared to influence the work reported in this paper.

Appendix A. Zernike graph

We evaluate three distinct strategies for organising Zernike graph: aberration grouping, azimuthal degree grouping, and a baseline with no grouping strategy. While the azimuthal degree grouping is detailed in the methodology section, here we discuss the aberration grouping approach and the baseline with no grouping.

Appendix A.1. Aberration group

Similar to Fig. 3 in the main paper, this framework follows the same four-stage architecture described in the methodology section but with aberration-based groups replacing azimuthal degree groups. By structuring the graph around aberration groups, the network explicitly learns how specific combinations of Zernike modes with similar optical physical effects collectively distort the wavefront and thereby facilitates effective aberration correction.

Appendix A.2. Baseline with no grouping strategy

In this baseline method, no grouping is applied; each node is initialised with its corresponding Zernike latent representation and exchanges information with all other Zernike modes through a fully connected graph structure. This fully connected approach does not explicitly model any physical relationships between the Zernike modes, providing a reference point for assessing the benefits of structured grouping strategies.

Appendix B. Implementation details of competing SOTA methods

We implemented DeblurGANv2 [34], MPRNet [67], Restormer [32], CascadedGaze [68], DiffIR [35], and KBNets (both large KBNets_L and small KBNets_S variants) [49] according to their official configurations. All these networks were originally designed for general image restoration tasks (e.g., denoising, deraining, deblurring); in our experiments, we adapted them to produce a single-channel restored optical image from the phase-diverse inputs and adjusted hyperparameters only when necessary to accommodate the larger dataset size and extended training duration.

For specialised aberration correction networks, we compared against DeAbe (RCAN) [22, 45] and SFT-DFCAN [25]. The DeAbe model employs a 3D Residual Channel Attention Networks (RCAN) to remove aberrations from 3D fluorescence microscopy stacks and then uses two additional networks to progressively improve image resolution and contrast. This 3D RCAN is adapted from the 2D RCAN, which was originally developed for image super-resolution on natural images. In our work, we used only the 2D RCAN variant. Following insights from the DeAbe paper that microscopy images

L_R	L_C	L_Z	PSNR	SSIM	LPIPS	Zernike RMS_{WFE} (rad)
✓			28.56	0.7795	0.3930	0.4542
	✓		28.55	0.7789	0.3947	0.4552
		✓	28.53	0.7779	0.3945	0.4551
✓	✓		28.57	0.7785	0.3938	0.4574
	✓	✓	28.54	0.7778	0.3947	0.4550
✓		✓	28.56	0.7794	0.3930	0.4506
✓	✓	✓	28.80	0.7843	0.3887	0.4374

Table B.4: Ablation analysis for FAA loss.

often have lower high-frequency content compared to natural images, we modified the network to process whole 256×256 phase-diverse images rather than patches, and adjusted the architecture to 5 residual groups and 10 residual blocks to accommodate the larger input size. The final layer of the network was further modified to output single-channel restored images.

For SFT-DFCAN [25], the original implementation requires first training SFE-Net to predict the PSF from aberrated images, then using both the aberrated image and estimated PSF as inputs to SFT-DFCAN to generate the super-resolved, aberration-corrected result. Given the complexity of our dataset and the authors’ demonstration that accurate PSF estimation is critical for successful microscopy image reconstruction, we modified our implementation to directly accept the ground truth 33×33 PSF together with the 256×256 phase-diverse input and then output the 256×256 restored single-channel image. This ensures a fair comparison by isolating the image restoration performance from potential errors in PSF estimation.

For networks that predict Zernike coefficients, we trained Swin Transformer (Base and Large variants) [69] following standard protocols. We adapted each backbone to accept the same 256×256 phase-diverse inputs and modified the final layers to regress 25 Zernike coefficients.

Appendix C. Ablation studies on FAA loss components

Table B.4 presents an ablation study evaluating the individual and combined effects of the three FAA loss components: Restoration loss (L_R), Cross-verification loss (L_C), and Zernike loss (L_Z). While individual components or pairs of two offer marginal gains, some combinations are counterproductive. The best performance is achieved when all three components are used together, confirming that the full FAA loss provides complementary, three-way supervision that effectively aligns image restoration with physically consistent Zernike prediction in the spatial frequency domain.

References

- [1] K. M. Hampson, R. Turcotte, D. T. Miller, K. Kurokawa, J. R. Males, N. Ji, M. J. Booth, Adaptive optics for high-resolution imaging, *Nature Reviews Methods Primers* 1 (1) (2021) 68.
- [2] M. Schwertner, M. J. Booth, M. A. Neil, T. Wilson, Measurement of specimen-induced aberrations of biological samples using phase stepping interferometry, *Journal of microscopy* 213 (1) (2004) 11–19.
- [3] J. W. Hardy, *Adaptive optics for astronomical telescopes*, Vol. 16, Oxford University Press on Demand, 1998.
- [4] B. C. Platt, R. Shack, *History and principles of shack-hartmann wavefront sensing* (2001).
- [5] X. Tao, B. Fernandez, O. Azucena, M. Fu, D. Garcia, Y. Zuo, D. C. Chen, J. Kubby, Adaptive optics confocal microscopy using direct wavefront sensing, *Optics letters* 36 (7) (2011) 1062–1064.
- [6] M. A. Vorontsov, G. W. Carhart, M. Cohen, G. Cauwenberghs, Adaptive optics based on analog parallel stochastic optimization: analysis and experimental demonstration, *JOSA A* 17 (8) (2000) 1440–1453.
- [7] S. Zommer, E. Ribak, S. Lipson, J. Adler, Simulated annealing in ocular adaptive optics, *Optics letters* 31 (7) (2006) 939–941.

- [8] P. Yang, M. Ao, Y. Liu, B. Xu, W. Jiang, Intracavity transverse modes controlled by a genetic algorithm based on zernike mode coefficients, *Optics express* 15 (25) (2007) 17051–17062.
- [9] R. W. Gerchberg, A practical algorithm for the determination of plane from image and diffraction pictures, *Optik* 35 (2) (1972) 237–246.
- [10] A. J. Janssen, Extended nijboer–zernike approach for the computation of optical point-spread functions, *JOSA A* 19 (5) (2002) 849–857.
- [11] J. Liu, P. Wang, X. Zhang, Y. He, X. Zhou, H. Ye, Y. Li, S. Xu, S. Chen, D. Fan, Deep learning based atmospheric turbulence compensation for orbital angular momentum beam distortion and communication, *Optics express* 27 (12) (2019) 16671–16688.
- [12] H. Guo, Y. Xu, Q. Li, S. Du, D. He, Q. Wang, Y. Huang, Improved machine learning approach for wavefront sensing, *Sensors* 19 (16) (2019) 3533.
- [13] K. Wang, M. Zhang, J. Tang, L. Wang, L. Hu, X. Wu, W. Li, J. Di, G. Liu, J. Zhao, Deep learning wavefront sensing and aberration correction in atmospheric turbulence, *Photonix* 2 (1) (2021) 1–11.
- [14] Y. Nishizaki, M. Valdivia, R. Horisaki, K. Kitaguchi, M. Saito, J. Tanida, E. Vera, Deep learning wavefront sensing, *Optics express* 27 (1) (2019) 240–251.
- [15] Y. Xu, D. He, Q. Wang, H. Guo, Q. Li, Z. Xie, Y. Huang, An improved method of measuring wavefront aberration based on image with machine learning in free space optical communication, *Sensors* 19 (17) (2019) 3665.
- [16] Q. Xin, G. Ju, C. Zhang, S. Xu, Object-independent image-based wavefront sensing approach using phase diversity images and deep learning, *Optics express* 27 (18) (2019) 26102–26119.
- [17] Q. Hu, M. Hailstone, J. Wang, M. Wincott, D. Stoychev, H. Atilgan, D. Gala, T. Chaiamarit, R. M. Parton, J. Antonello, et al., Universal adaptive optics for microscopy through embedded neural network control, *arXiv preprint arXiv:2301.02647* (2023).

- [18] M. R. Rai, C. Li, H. T. Ghashghaei, A. Greenbaum, Deep learning-based adaptive optics for light sheet fluorescence microscopy, *Biomedical Optics Express* 14 (6) (2023) 2905–2919.
- [19] D. Fish, A. Brinicombe, E. Pike, J. Walker, Blind deconvolution by means of the richardson–lucy algorithm, *JOSA A* 12 (1) (1995) 58–65.
- [20] A. Shajkofci, M. Liebling, Semi-blind spatially-variant deconvolution in optical microscopy with local point spread function estimation by use of convolutional neural networks, in: 2018 25th IEEE International Conference on Image Processing (ICIP), IEEE, 2018, pp. 3818–3822.
- [21] R. K. Tyson, B. W. Frazier, *Principles of adaptive optics*, CRC press, 2022.
- [22] M. Guo, Y. Wu, C. M. Hobson, Y. Su, S. Qian, E. Krueger, R. Christensen, G. Kroeschell, J. Bui, M. Chaw, et al., Deep learning-based aberration compensation improves contrast and resolution in fluorescence microscopy, *Nature Communications* 16 (1) (2025) 313.
- [23] A. P. Krishnan, C. Belthangady, C. Nyby, M. Lange, B. Yang, L. A. Royer, Optical aberration correction via phase diversity and deep learning, *BioRxiv* (2020) 2020–04.
- [24] I. Kang, Q. Zhang, S. X. Yu, N. Ji, Coordinate-based neural representations for computational adaptive optics in widefield microscopy, *arXiv preprint arXiv:2307.03812* (2023).
- [25] C. Qiao, H. Chen, R. Wang, T. Jiang, Y. Wang, D. Li, Deep learning-based optical aberration estimation enables offline digital adaptive optics and super-resolution imaging, *Photonics Research* 12 (3) (2024) 474–484.
- [26] M. Schwertner, M. Booth, T. Wilson, Simulation of specimen-induced aberrations for objects with spherical and cylindrical symmetry, *Journal of microscopy* 215 (3) (2004) 271–280.

- [27] K. Wang, W. Sun, C. T. Richie, B. K. Harvey, E. Betzig, N. Ji, Direct wavefront sensing for high-resolution in vivo imaging in scattering tissue, *Nature communications* 6 (1) (2015) 7276.
- [28] M. J. Booth, Adaptive optical microscopy: the ongoing quest for a perfect image, *Light: Science & Applications* 3 (4) (2014) e165–e165.
- [29] S. B. Z. Hua, A. X. Lu, A. M. Moses, Cytoimagenet: A large-scale pretraining dataset for bioimage transfer learning, *arXiv preprint arXiv:2111.11646* (2021).
- [30] J. Liang, J. Cao, G. Sun, K. Zhang, L. Van Gool, R. Timofte, Swinir: Image restoration using swin transformer, in: *Proceedings of the IEEE/CVF international conference on computer vision*, 2021, pp. 1833–1844.
- [31] Z. Wang, X. Cun, J. Bao, W. Zhou, J. Liu, H. Li, Uformer: A general u-shaped transformer for image restoration, in: *Proceedings of the IEEE/CVF conference on computer vision and pattern recognition*, 2022, pp. 17683–17693.
- [32] S. W. Zamir, A. Arora, S. Khan, M. Hayat, F. S. Khan, M.-H. Yang, Restormer: Efficient transformer for high-resolution image restoration, in: *Proceedings of the IEEE/CVF conference on computer vision and pattern recognition*, 2022, pp. 5728–5739.
- [33] S. W. Zamir, A. Arora, S. Khan, M. Hayat, F. S. Khan, M.-H. Yang, L. Shao, Multi-stage progressive image restoration, in: *Proceedings of the IEEE/CVF conference on computer vision and pattern recognition*, 2021, pp. 14821–14831.
- [34] O. Kupyn, T. Martyniuk, J. Wu, Z. Wang, Deblurgan-v2: Deblurring (orders-of-magnitude) faster and better, in: *Proceedings of the IEEE/CVF international conference on computer vision*, 2019, pp. 8878–8887.
- [35] B. Xia, Y. Zhang, S. Wang, Y. Wang, X. Wu, Y. Tian, W. Yang, L. Van Gool, Diffir: Efficient diffusion model for image restoration, in: *Proceedings of the IEEE/CVF International Conference on Computer Vision*, 2023, pp. 13095–13105.

- [36] Z. Lu, Y. Liu, M. Jin, X. Luo, H. Yue, Z. Wang, S. Zuo, Y. Zeng, J. Fan, Y. Pang, et al., Virtual-scanning light-field microscopy for robust snapshot high-resolution volumetric imaging, *Nature Methods* 20 (5) (2023) 735–746.
- [37] X. Qin, Z. Wang, Y. Bai, X. Xie, H. Jia, Ffa-net: Feature fusion attention network for single image dehazing, in: *Proceedings of the AAAI conference on artificial intelligence*, Vol. 34, 2020, pp. 11908–11915.
- [38] Y. Song, Z. He, H. Qian, X. Du, Vision transformers for single image dehazing, *IEEE Transactions on Image Processing* 32 (2023) 1927–1941.
- [39] W. Yinglong, H. Bin, Casdyf-net: Image dehazing via cascaded dynamic filters, *arXiv preprint arXiv:2409.08510* (2024).
- [40] B. Lim, S. Son, H. Kim, S. Nah, K. Mu Lee, Enhanced deep residual networks for single image super-resolution, in: *Proceedings of the IEEE conference on computer vision and pattern recognition workshops*, 2017, pp. 136–144.
- [41] X. Wang, L. Xie, C. Dong, Y. Shan, Real-esrgan: Training real-world blind super-resolution with pure synthetic data, in: *Proceedings of the IEEE/CVF international conference on computer vision*, 2021, pp. 1905–1914.
- [42] C.-C. Hsu, C.-M. Lee, Y.-S. Chou, Drct: Saving image super-resolution away from information bottleneck, *arXiv preprint arXiv:2404.00722* (2024).
- [43] J. Su, B. Xu, H. Yin, A survey of deep learning approaches to image restoration, *Neurocomputing* 487 (2022) 46–65.
- [44] X. Mao, C. Shen, Y.-B. Yang, Image restoration using very deep convolutional encoder-decoder networks with symmetric skip connections, *Advances in neural information processing systems* 29 (2016).
- [45] Y. Zhang, K. Li, K. Li, L. Wang, B. Zhong, Y. Fu, Image super-resolution using very deep residual channel attention networks, in: *Proceedings of the European conference on computer vision (ECCV)*, 2018, pp. 286–301.

- [46] D. Wang, J.-S. Pan, J.-H. Tang, Single image deraining using residual channel attention networks, *Journal of Computer Science and Technology* 38 (2) (2023) 439–454.
- [47] S. Guo, H. Yong, X. Zhang, J. Ma, L. Zhang, Spatial-frequency attention for image denoising, *arXiv preprint arXiv:2302.13598* (2023).
- [48] K. Purohit, M. Suin, A. Rajagopalan, V. N. Boddeti, Spatially-adaptive image restoration using distortion-guided networks, in: *Proceedings of the IEEE/CVF international conference on computer vision*, 2021, pp. 2309–2319.
- [49] Y. Zhang, D. Li, X. Shi, D. He, K. Song, X. Wang, H. Qin, H. Li, Kbnnet: Kernel basis network for image restoration, *arXiv preprint arXiv:2303.02881* (2023).
- [50] Y. Zhang, K. Li, K. Li, B. Zhong, Y. Fu, Residual non-local attention networks for image restoration, *arXiv preprint arXiv:1903.10082* (2019).
- [51] S. W. Zamir, A. Arora, S. Khan, M. Hayat, F. S. Khan, M.-H. Yang, L. Shao, Learning enriched features for real image restoration and enhancement, in: *Computer Vision—ECCV 2020: 16th European Conference, Glasgow, UK, August 23–28, 2020, Proceedings, Part XXV* 16, Springer, 2020, pp. 492–511.
- [52] J. Liu, Q. Wang, H. Fan, Y. Wang, Y. Tang, L. Qu, Residual denoising diffusion models, in: *Proceedings of the IEEE/CVF Conference on Computer Vision and Pattern Recognition*, 2024, pp. 2773–2783.
- [53] Z. Yue, K. Liao, C. C. Loy, Arbitrary-steps image super-resolution via diffusion inversion, *arXiv preprint arXiv:2412.09013* (2024).
- [54] J. W. Goodman, *Introduction to Fourier Optics*, Roberts and Company Publishers, 2005.
- [55] R. J. Noll, Zernike polynomials and atmospheric turbulence, *JOsA* 66 (3) (1976) 207–211.

- [56] D. Saha, U. Schmidt, Q. Zhang, A. Barbotin, Q. Hu, N. Ji, M. J. Booth, M. Weigert, E. W. Myers, Practical sensorless aberration estimation for 3d microscopy with deep learning, *Optics express* 28 (20) (2020) 29044–29053.
- [57] Y. E. Kok, A. Bentley, A. J. Parkes, M. G. Somekh, A. J. Wright, M. P. Pound, Practical aberration correction using deep transfer learning with limited experimental data, *Optics Express* 33 (6) (2025) 14431–14444.
- [58] P. Velickovic, G. Cucurull, A. Casanova, A. Romero, P. Lio, Y. Bengio, et al., Graph attention networks, *stat* 1050 (20) (2017) 10–48550.
- [59] B. Deng, S. Song, A. P. French, D. Schluppeck, M. P. Pound, Advancing saliency ranking with human fixations: Dataset models and benchmarks, in: *Proceedings of the IEEE/CVF Conference on Computer Vision and Pattern Recognition*, 2024, pp. 28348–28357.
- [60] E. Williams, J. Moore, S. W. Li, G. Rustici, A. Tarkowska, A. Chessel, S. Leo, B. Antal, R. K. Ferguson, U. Sarkans, et al., Image data resource: a bioimage data integration and publication platform, *Nature methods* 14 (8) (2017) 775–781.
- [61] V. Ljosa, K. L. Sokolnicki, A. E. Carpenter, Annotated high-throughput microscopy image sets for validation., *Nature methods* 9 (7) (2012) 637–637.
- [62] Q. Huynh-Thu, M. Ghanbari, Scope of validity of psnr in image/video quality assessment, *Electronics letters* 44 (13) (2008) 800–801.
- [63] Z. Wang, A. C. Bovik, H. R. Sheikh, E. P. Simoncelli, Image quality assessment: from error visibility to structural similarity, *IEEE transactions on image processing* 13 (4) (2004) 600–612.
- [64] R. Zhang, P. Isola, A. A. Efros, E. Shechtman, O. Wang, The unreasonable effectiveness of deep features as a perceptual metric, in: *Proceedings of the IEEE conference on computer vision and pattern recognition*, 2018, pp. 586–595.
- [65] xiaoju ye, calflops: a flops and params calculate tool for neural networks in pytorch framework (2023).
URL <https://github.com/MrYxJ/calculate-flops.pytorch>

- [66] A. Maréchal, Study of the combined effects of diffraction and geometrical aberrations on the image of a luminous point, *Rev. Opt. Theor. Instrum* 26 (1947) 257.
- [67] A. Mehri, P. B. Ardakani, A. D. Sappa, Mprnet: Multi-path residual network for lightweight image super resolution, in: *Proceedings of the IEEE/CVF Winter Conference on Applications of Computer Vision*, 2021, pp. 2704–2713.
- [68] A. Ghasemabadi, M. K. Janjua, M. Salameh, C. Zhou, F. Sun, D. Niu, Cascad-edgaze: Efficiency in global context extraction for image restoration, *arXiv preprint arXiv:2401.15235* (2024).
- [69] Z. Liu, Y. Lin, Y. Cao, H. Hu, Y. Wei, Z. Zhang, S. Lin, B. Guo, Swin transformer: Hierarchical vision transformer using shifted windows, in: *Proceedings of the IEEE/CVF international conference on computer vision*, 2021, pp. 10012–10022.